DELFT UNIVERSITY OF TECHNOLOGY

REPORT 06 - 15

A Note on the Numerical Simulation of Kleijn's Benchmark Problem

S. van Veldhuizen, C. Vuik, C.R. Kleijn

ISSN 1389-6520

Reports of the Department of Applied Mathematical Analysis

Delft 2006

A Note on the Numerical Simulation of Kleijn's Benchmark Problem

S. van Veldhuizen* C. Vuik* C.R. Kleijn†

Abstract

In this study various numerical schemes for transient simulations of 2D laminar reacting gas flows, as typically found in Chemical Vapor Deposition (CVD) reactors, are proposed and compared. These systems are generally modeled by means of many stiffly coupled elementary gas phase reactions between a large number of reactants and intermediate species. The purpose of this study is to develop robust and efficient solvers for the stiff reaction system, where as a first approach the velocity and temperature fields are assumed to be given. Furhtermore, we neglect thermal diffusion (Soret effect). In this paper we mainly focus on the performance of different time integration methods, and their properties to successfully solve the transient problem. Besides stability, which is important due to the stiffness of the problem, the preservation of non-negativity of the species is crucial. It appears that this extra condition on time integration methods is much more restrictive towards the time-step than stability.

1 Introduction

This report is a continuation of the previous report [12], in which a 'small' Chemical Vapor Deposition (CVD) problem was solved. In [12] four different (higher order) time integration methods are compared in terms of efficiency for transient simulations running into steady state. As iterative nonlinear solver we use the full Newton iteration, whereas to solve linear systems a direct solver has been used. In this paper we will simulate instead of simple CVD systems as has been done in [12], the well known benchmark problem of Kleijn [8]. The transport and chemistry model used in this benchmark will be discussed in the next sections, and can also be found in [8].

Chemical vapor deposition is extensively described in, for example, [3]. More information on the mathematical model of CVD can be found in [5, 7, 6]. A shorter note on the mathematical model of CVD is, for instance, [11, 12].

*Delft University of Technology, Delft Institute of Applied Mathematics, Mekelweg 4, 2628 CD Delft, The Netherlands (s.vanveldhuizen@tudelft.nl, c.vuik@tudelft.nl)

†Delft University of Technology, Department of Multi Scale Physics, Prins Bernardlaan 6, 2628 BW Delft, The Netherlands (c.r.kleijn@tudelft.nl)

2 Transport Model

The mathematical model describing the CVD process consists of a set of partial differential equations with appropriate boundary conditions, which describe the gas flow, the transport of energy, the transport of species and the chemical reactions in the reactor.

The gas mixture in the reactor is assumed to behave as a continuum. This assumption is only valid when the mean free path of the molecules is much smaller than a characteristic dimension of the reactor. For Knudsen numbers $\mathrm{Kn} < 0.01$, where

$$\mathrm{Kn} = \frac{\xi}{L}, \tag{1}$$

the gas mixture behaves as a continuum. In (1) ξ is the mean free path length of the molecules and L a typical characteristic dimension of the reactor. For pressures larger than 100 Pa and typical reactor dimensions larger than 0.01 m the continuum approach can be used safely. See, for example, [5].

Furthermore, the gas mixture is assumed to behave as an ideal and transparent gas[1] behaving in accordance with Newton's law of viscosity. The gas flow in the reactor is assumed to be laminar (low Reynolds number flow). Since no large velocity gradients appear in CVD gas flows, viscous heating due to dissipation will be neglected. We also neglect the effects of pressure variations in the energy equation.

The composition of the N component gas mixture is described in terms of the dimensionless mass fractions $\omega_i = \frac{\rho_i}{\rho}$, $i = 1, \ldots, N$, having the property

$$\sum_{i=1}^{N} \omega_i = 1. \tag{2}$$

The transport of mass, momentum and heat are described respectively by the continuity equation (3), the Navier-Stokes equations (4) and the transport equation for thermal energy (5) expressed in terms of temperature T:

$$\frac{\partial \rho}{\partial t} = -\nabla \cdot (\rho \mathbf{v}), \tag{3}$$

$$\frac{\partial (\rho \mathbf{v})}{\partial t} = -(\nabla \rho \mathbf{v}) \cdot \mathbf{v} + \nabla \cdot \left[\mu \left(\nabla \mathbf{v} + (\nabla \mathbf{v})^{\mathbf{T}} \right) - \frac{\mathbf{2}}{\mathbf{3}} \mu (\nabla \cdot \mathbf{v}) \mathbf{I} \right] - \nabla \mathbf{P} + \rho \mathbf{g}, \tag{4}$$

$$\begin{aligned} c_p \frac{\partial (\rho T)}{\partial t} &= -c_p \nabla \cdot (\rho \mathbf{v} T) + \nabla \cdot (\lambda \nabla T) + \\ &\quad + \nabla \cdot \left(RT \sum_{i=1}^{N} \frac{\mathbb{D}_i^T}{M_i} \frac{\nabla f_i}{f_i} \right) + \sum_{i=1}^{N} \frac{H_i}{m_i} \nabla \cdot \mathbf{j}_i \\ &\quad - \sum_{i=1}^{N} \sum_{k=1}^{K} H_i \nu_{ik} R_k^g, \end{aligned} \tag{5}$$

[1] By transparent we mean that the adsorption of heat radiation by the gas(es) will be small.

with ρ gas mixture density, $\mathbf{v}$ mass averaged velocity vector, μ the viscosity, $\mathbf{I}$ the unit tensor, $\mathbf{g}$ gravity acceleration, c_p specific heat ($\frac{\mathrm{J}}{\mathrm{mol\,K}}$), λ the thermal conductivity ($\frac{\mathrm{W}}{\mathrm{m\,K}}$) and R the gas constant. Gas species i has a mole fraction f_i, a molar mass m_i, a thermal diffusion coefficient $\mathbb{D}_i^T$, a molar enthalpy H_i and a diffusive mass flux $\mathbf{j}_i$. The stoichiometric coefficient of the i^{th} species in the k^{th} gas-phase reaction with net molar reaction rate R_k^g is ν_{ik}.

We assume that in the gas-phase K reversible reactions take place. For the k^{th} reaction the *net* molar reaction rate is denoted as R_k^g $\left(\frac{\text{mole}}{\mathrm{m^3\,s}}\right)$. In Section 3 the chemistry model is discussed and in particular the net molar reaction rate will be defined.

The balance equation for the i^{th} gas species, $i = 1, \ldots, N$, in terms of mass fractions and diffusive mass fluxes is then given as

$$\frac{\partial(\rho\omega_i)}{\partial t} = -\nabla\cdot(\rho\mathbf{v}\omega_i) - \nabla\cdot\mathbf{j}_i + m_i\sum_{k=1}^{K}\nu_{ik}R_k^g, \tag{6}$$

where $\mathbf{j}_i$ is the diffusive flux. The mass diffusion flux is composed of concentration diffusion and thermal diffusion, e.g.,

$$\mathbf{j}_i = \mathbf{j}_i^C + \mathbf{j}_i^T. \tag{7}$$

The first type of diffusion, $\mathbf{j}_i^C$, occurs as a result of a concentration gradient in the system. Thermal diffusion is the kind of diffusion resulting from a temperature gradient. For a multicomponent gas mixture there are two approaches for the treatment of concentration diffusion, namely the full Stefan-Maxwell equations and an alternative approximation derived by Wilke using effective diffusion coefficients, see [5]. In this paper, we use the approach of effective diffusion coefficients. Then, the species concentration equations reduce to

$$\begin{aligned}\frac{\partial(\rho\omega_i)}{\partial t} &= -\nabla\cdot(\rho\mathbf{v}\omega_i) + \nabla\cdot(\rho\mathbb{D}_i'\nabla\omega_i) + \nabla\cdot(\mathbb{D}_i^T\nabla(\ln T)) + \\ &\quad + m_i\sum_{k=1}^{K}\nu_{ik}R_k^g,\end{aligned} \tag{8}$$

where $\mathbb{D}_i'$ is an effective diffusion coefficient for species i and $\mathbb{D}_i^T$ the multi-component thermal diffusion coefficient for species i.

The main focus of our research is on efficient solvers for the species equation(s) (8). Typically the time scales of the slow and fast reaction terms differ orders of magnitude from each other and from the time scales of the diffusion and advection terms, leading to extremely stiff systems.

2.1 Simplified Model

In this paper we will solve the coupled system of N species equations (8), where N denotes the number of gas-species in the reactor. Note that it suffices to solve the $(N-1)$

coupled species equations for all species except the carrier gas, where its mass fraction $\omega_{\text{carrier gas}}$ will be computed via the property

$$\sum_{i=1}^{N} \omega_i = 1. \tag{9}$$

For the moment we only focus on the development of efficient solvers for species equations, because solving the system of equations (3) - (5) is a rather trivial task in comparison with solving the system of species equations (6). Therefore, we assume that both the velocity field, temperature field, pressure field and density field are given. To be more precise, they are computed via using software developed by Kleijn [8].

With respect to the mass diffusion fluxes, we remark that the thermal diffusion flux is omitted. The concentration mass diffusion fluxes are described by effective diffusion coefficients as

$$j_i^C = \rho \mathbb{D}_{i,\text{He}} \nabla \omega_i, \tag{10}$$

where, according to [8]

$$\mathbb{D}_{i,\text{He}} = \varpi T^{\varrho}, \tag{11}$$

and the fitting constants ϖ and ϱ as in Table 1.

Species	ϖ $\left[\frac{\text{m}^2}{\text{s K}^{\varrho_D}}\right]$	ϱ	Species	ϖ $\left[\frac{\text{m}^2}{\text{s K}^{\varrho_D}}\right]$	ϱ
H	1.94×10^{-8}	1.67	Si_2H_2	3.67×10^{-9}	1.67
H_2	1.29×10^{-8}	1.65	Si_2H_3	3.56×10^{-9}	1.67
Si	2.91×10^{-9}	1.75	H_2SiSiH_2	3.46×10^{-9}	1.67
SiH	5.56×10^{-9}	1.66	H_3SiSiH	3.46×10^{-9}	1.67
SiH_2	4.95×10^{-9}	1.67	Si_2H_5	3.35×10^{-9}	1.67
SiH_3	4.60×10^{-9}	1.67	Si_2H_6	3.26×10^{-9}	1.67
SiH_4	4.28×10^{-9}	1.67	Si_3	2.23×10^{-9}	1.75
Si_2	2.47×10^{-9}	1.75	Si_3H_8	2.64×10^{-9}	1.67

Table 1: Fitted diffusion constants of the various species in the gas mixture in the simplified model

3 Gas Phase Reaction Model

In the region above the hot susceptor the reactive gas silane SiH_4 decomposes into disilane SiH_2 and hydrogen gas H_2. This gas phase reaction initiates a chain of homogeneous reactions leading to the formation (and deformation) of silicon containing gases. Each of these species may diffuse to the reacting surface and react to solid silicon.

In this paper we have used the chemistry model by Coltrin et. al. [2], which is also used in [8]. The gas mixture contains besides the carrier gas helium He also the species given in Table 2.

Species	Molar Mass $[\frac{\text{kg}}{\text{mole}}]$	Species	Molar Mass $[\frac{\text{kg}}{\text{mole}}]$
H	0.001008	Si_2H_2	0.058188
H_2	0.002016	Si_2H_3	0.059196
Si	0.028086	H_2SiSiH_2	0.060204
SiH	0.029094	H_3SiSiH	0.060204
SiH_2	0.030102	Si_2H_5	0.061212
SiH_3	0.031110	Si_2H_6	0.062219
SiH_4	0.032118	Si_3	0.084258
Si_2	0.056172	Si_3H_8	0.092321

Table 2: Mole mass of the species in the gas mixture

The 26 reversible gas phase reactions in this model are listed in Table 3. Since different species can act as reactant and as product, the gas phase can be written in the general form

$$\sum_{\text{reactants}} \| - \nu_{ik}\| \mathcal{A}_i \overset{k^g_{k,\text{forward}}}{\underset{k^g_{k,\text{backward}}}{\rightleftarrows}} \sum_{\text{products}} \|\nu_{ik}\| \mathcal{A}_i. \tag{12}$$

In (12) $\mathcal{A}_i$ represent the different gaseous species in the reactor chamber, $k^g_{k,\text{forward}}$ the forward reaction rate constant and $k^g_{k,\text{backward}}$ the backward reaction rate constant. By taking

$$\begin{aligned} &\nu_{ik} > 0 \text{ for the products of the forward reaction} \\ &\nu_{ik} < 0 \text{ for the reactants of the forward reaction} \end{aligned}$$

and

$$\begin{aligned} \|\nu_{ik}\| = \nu_{ik} \quad &\text{and} \quad \| - \nu_{ik}\| = 0 \qquad \text{for} \quad \nu_{ik} \geq 0 \\ \|\nu_{ik}\| = 0 \quad &\text{and} \quad \| - \nu_{ik}\| = |\nu_{ik}| \quad \text{for} \quad \nu_{ik} \leq 0 \end{aligned}$$

equation (12) represents a general equilibrium reaction. The net reaction rate R^g_k for the k^{th} reaction is given by

$$\begin{aligned} R^g_k &= R^{g,\text{forward}}_k - R^{g,\text{backward}}_k = \\ &= k^g_{k,\text{forward}} \prod_{i=1}^{N} \left(\frac{Pf_i}{RT}\right)^{\|-\nu_{ik}\|} - k^g_{k,\text{backward}} \prod_{i=1}^{N} \left(\frac{Pf_i}{RT}\right)^{\|\nu_{ik}\|}. \end{aligned} \tag{13}$$

The forward reaction rate constants are fitted according to the Modified Law of Arrhenius, i.e.,

$$k^g_{k,\text{forward}}(T) = A_k T^{\beta_k} e^{\frac{-E_k}{RT}}, \tag{14}$$

where the values of A_k, β_k and E_k are listed in Table 3. The backward reaction rate constants have to be calculated self consistently from the forward reaction rate constants and reaction thermo-chemistry as

$$k^g_{k,\text{backward}}(T) = \frac{k^g_{k,\text{forward}}(T)}{K^g_k} \left(\frac{RT}{P^0}\right)^{\sum_i \nu_{ik}}, \tag{15}$$

with K^g_k the reaction equilibrium constant given by

$$K^g_k(T) = e^{-\frac{\Delta H^0_k(T) - T\Delta S^0_k(T)}{RT}}, \text{ with} \tag{16}$$

$$\Delta H^0_k(T) = \sum_{i=1}^{N} \nu_{ik} H^0_i(T), \text{ and,} \tag{17}$$

$$\Delta S^0_k(T) = \sum_{i=1}^{N} \nu_{ik} S^0_i(T). \tag{18}$$

3.1 Simplified Chemistry Model

Instead of computing the backward reaction rate constants via (15) - (18), we use, following [8], approximate temperature fits for the equilibrium constants of the form

$$K^g_k(T) = A_{k,eq} T^{\beta_{k,eq}} e^{\frac{-E_{k,eq}}{RT}}. \tag{19}$$

The values for $A_{k,eq}$, $\beta_{k,eq}$ and $E_{k,eq}$ can be found in Table 4, which is taken from [8].

4 Surface Reaction Model

At the reacting surface S irreversible reactions take place, such that gaseous reactants will be transformed into solid and gaseous reaction products. The reactions that take place are of the form

$$\sum_{i=1}^{N} \|-\sigma_{is}\| \mathcal{A}_i \xrightarrow{R^S_s} \sum_{i=1}^{N} \|-\sigma_{is}\| \mathcal{A}_i + \sum_{j=1}^{M} \chi_{js} \mathcal{B}_j, \tag{20}$$

where $\mathcal{A}_i$, $i = 1, \ldots, N$, is a gaseous reactant, and $\mathcal{B}_j$, $j = 1, \ldots, M$, a *solid* reaction product. In (20) σ_{is} and χ_{js} are the stoichiometric coefficients for the gaseous and solid species for surface reaction s, where $s = 1, \ldots, S$. For the definition of $\|\sigma_{is}\|$ the same convention as in Section 3 has been taken.

In the problem that we discuss in this paper solid silicon atoms Si are deposited on the wafer surface. Deposition of the solid silicon Si (s) is due to one of the surface reactions:

$$\text{Si}_n\text{H}_{2m} \xrightarrow{R^S_{\text{Si}_n\text{H}_{2m}}} n \text{ Si (s)} + m \text{ H}_2 \text{ (g)}, \tag{21}$$

$$\text{Si}_n\text{H}_{2m+1} \xrightarrow{R^S_{\text{Si}_n\text{H}_{2m+1}}} n \text{ Si (s)} + m \text{ H}_2 \text{ (g)} + \text{H (g)}, \tag{22}$$

k	Reaction	A_k (-)	β_k (-)	E_k ($\frac{\text{kJ}}{\text{mol}}$)
1	$SiH_4 \rightleftharpoons SiH_2 + H_2$	1.09×10^{25}	-3.37	256
2	$SiH_4 \rightleftharpoons SiH_3 + H$	3.69×10^{15}	0.0	390
3	$Si_2H_6 \rightleftharpoons SiH_4 + SiH_2$	3.24×10^{29}	-4.24	243
4	$SiH_4 + H \rightleftharpoons SiH_3 + H_2$	1.46×10^{7}	0.0	10
5	$SiH_4 + SiH_3 \rightleftharpoons Si_2H_5 + H_2$	1.77×10^{6}	0.0	18
6	$SiH_4 + SiH \rightleftharpoons Si_2H_3 + H_2$	1.45×10^{6}	0.0	8
7	$SiH_4 + SiH \rightleftharpoons Si_2H_5$	1.43×10^{7}	0.0	8
8	$SiH_2 \rightleftharpoons Si + H_2$	1.06×10^{14}	-0.88	189
9	$SiH_2 + H \rightleftharpoons SiH + H_2$	1.39×10^{7}	0.0	8
10	$SiH_2 + H \rightleftharpoons SiH_3$	3.81×10^{7}	0.0	8
11	$SiH_2 + SiH_3 \rightleftharpoons Si_2H_5$	6.58×10^{6}	0.0	8
12	$SiH_2 + Si_2 \rightleftharpoons Si_3 + H_2$	3.55×10^{5}	0.0	8
13	$SiH_2 + Si_3 \rightleftharpoons Si_2H_2 + Si_2$	1.43×10^{5}	0.0	68
14	$H_2SiSiH_2 \rightleftharpoons Si_2H_2 + H_2$	3.16×10^{14}	0.0	222
15	$Si_2H_6 \rightleftharpoons H_3SiSiH + H_2$	7.94×10^{15}	0.0	236
16	$H_2 + SiH \rightleftharpoons SiH_3$	3.45×10^{7}	0.0	8
17	$H_2 + Si_2 \rightleftharpoons Si_2H_2$	1.54×10^{7}	0.0	8
18	$H_2 + Si_2 \rightleftharpoons 2\ SiH$	1.54×10^{7}	0.0	168
19	$H_2 + Si_3 \rightleftharpoons Si + Si_2H_2$	9.79×10^{6}	0.0	198
20	$Si_2H_5 \rightleftharpoons Si_2H_3 + H_2$	3.16×10^{14}	0.0	222
21	$Si_2H_2 + H \rightleftharpoons Si_2H_3$	8.63×10^{8}	0.0	8
22	$H + Si_2 \rightleftharpoons SiH + Si$	5.15×10^{7}	0.0	22
23	$SiH_4 + H_3SiSiH \rightleftharpoons Si_3H_8$	6.02×10^{7}	0.0	0
24	$SiH_2 + Si_2H_6 \rightleftharpoons Si_3H_8$	1.81×10^{8}	0.0	0
25	$SiH_3 + Si_2H_5 \rightleftharpoons Si_3H_8$	3.31×10^{7}	0.0	0
26	$H_3SiSiH \rightleftharpoons H_2SiSiH_2$	1.15×10^{20}	-3.06	28

Table 3: Fit parameters for gas phase forward reaction rate constants in the simplified model

where $n = 1, 2, 3$ and $m = 0, 1, 2, 3, 4$. In surface reactions (21) and (22) we have besides the deposition of silicon also desorption of gaseous hydrogen. From reactions (21) - (22) the stoichiometric coefficients σ_{is} and χ_{js} will follow immediately. In Table 5 a complete overview of the surface reactions for Kleijn's Benchmark problem is presented. The molar

k	Reaction	$A_{k,eq}$ (-)	$\beta_{k,eq}$ (-)	$E_{k,eq}$ ($\frac{\text{kJ}}{\text{mol}}$)
1	$SiH_4 \rightleftharpoons SiH_2 + H_2$	6.85×10^5	0.48	235
2	$SiH_4 \rightleftharpoons SiH_3 + H$	1.45×10^4	0.90	382
3	$Si_2H_6 \rightleftharpoons SiH_4 + SiH_2$	1.96×10^{12}	-1.68	229
4	$SiH_4 + H \rightleftharpoons SiH_3 + H_2$	1.75×10^3	-0.55	-50
5	$SiH_4 + SiH_3 \rightleftharpoons Si_2H_5 + H_2$	1.12×10^{-6}	2.09	-6
6	$SiH_4 + SiH \rightleftharpoons Si_2H_3 + H_2$	1.82×10^{-4}	1.65	21
7	$SiH_4 + SiH \rightleftharpoons Si_2H_5$	1.49×10^{-10}	1.56	-190
8	$SiH_2 \rightleftharpoons Si + H_2$	1.23×10^2	0.97	180
9	$SiH_2 + H \rightleftharpoons SiH + H_2$	2.05×10^1	-0.51	-101
10	$SiH_2 + H \rightleftharpoons SiH_3$	2.56×10^{-3}	-1.03	-285
11	$SiH_2 + SiH_3 \rightleftharpoons Si_2H_5$	1.75×10^{-12}	1.60	-241
12	$SiH_2 + Si_2 \rightleftharpoons Si_3 + H_2$	5.95×10^{-6}	1.15	-225
13	$SiH_2 + Si_3 \rightleftharpoons Si_2H_2 + Si_2$	2.67×10^0	-0.18	59
14	$H_2SiSiH_2 \rightleftharpoons Si_2H_2 + H_2$	1.67×10^6	-0.37	112
15	$Si_2H_6 \rightleftharpoons H_3SiSiH + H_2$	1.17×10^9	-0.36	235
16	$H_2 + SiH \rightleftharpoons SiH_3$	1.42×10^{-4}	-0.52	-183
17	$H_2 + Si_2 \rightleftharpoons Si_2H_2$	7.47×10^{-6}	-0.37	-216
18	$H_2 + Si_2 \rightleftharpoons 2\ SiH$	1.65×10^3	-0.91	180
19	$H_2 + Si_3 \rightleftharpoons Si + Si_2H_2$	1.55×10^2	-0.55	189
20	$Si_2H_5 \rightleftharpoons Si_2H_3 + H_2$	1.14×10^6	0.08	210
21	$Si_2H_2 + H \rightleftharpoons Si_2H_3$	3.43×10^{-4}	-0.31	-149
22	$H + Si_2 \rightleftharpoons SiH + Si$	1.19×10^3	-0.88	29
23	$SiH_4 + H_3SiSiH \rightleftharpoons Si_3H_8$	7.97×10^{-16}	2.48	-233
24	$SiH_2 + Si_2H_6 \rightleftharpoons Si_3H_8$	1.36×10^{-12}	1.64	-233
25	$SiH_3 + Si_2H_5 \rightleftharpoons Si_3H_8$	1.06×10^{-14}	1.85	-318
26	$H_3SiSiH \rightleftharpoons H_2SiSiH_2$	9.58×10^{-3}	0.50	-50

Table 4: Fit parameters for gas phase equilibrium constants in the simplified model

reaction rate R_i^S for the decomposition of gas species i is given as

$$R_i^S = \frac{\gamma_i}{1 - \frac{\gamma_i}{2}} \frac{P f_i}{(2\pi m_i R T_s)^{\frac{1}{2}}}, \tag{23}$$

where γ_i is the sticking coefficient of species i, and T_s the temperature of the wafer surface.

The sticking coefficients are for all silicon containing species equal to one, except for

$$\begin{aligned}\gamma_{\mathrm{Si_3H_8}} &= 0,\\ \gamma_{\mathrm{Si_2H_6}} &= 0.537e^{\frac{-9400}{T_s}}, \text{ and}\\ \gamma_{\mathrm{SiH_4}} &= \frac{1}{10}\gamma_{\mathrm{Si_2H_6}}.\end{aligned}$$

From (20) the growth rate $\mathcal{G}_j$ of solid species $\mathcal{B}_j$ can be deduced as

$$\mathcal{G}_j = 10^9 \frac{m_j}{\rho_j} \sum_{s=1}^{S} R_s^S \chi_{j,s}, \tag{24}$$

where ρ_j is its density in solid phase. The unit of the growth rate $\mathcal{G}_j$ is $\frac{\mathrm{nm}}{\mathrm{s}}$. In this paper we have as solid species solid silicon only. Consequently, only one growth rate has to be computed. The density of solid silicon[2] is

$$\rho_{\mathrm{Si}} = 2329 \quad \frac{\mathrm{kg}}{\mathrm{m}^3}. \tag{25}$$

More background information can be found in [5, 8].

4.1 Corresponding Boundary Conditions

On the reacting surface will be a net mass production $\mathcal{P}_i$. For ω_i this net mass production is given by

$$\mathcal{P}_i = m_i \sum_{s=1}^{S} \sigma_{is} R_s^S,$$

where m_i is the molar mass, σ_{is} the stoichiometric coefficient for the gaseous and solid species for surface reaction s ($s = 1, \ldots, S$) and R_s^S the reaction rate of reaction s on the surface.

We assume the no-slip condition on the wafer surface. Since there is mass production in normal direction the normal component of the velocity will not be equal to zero. We find for the velocity the boundary conditions

$$\begin{aligned}\mathbf{n}\cdot\mathbf{v} &= \frac{1}{\rho}\sum_{i=1}^{N} m_i \sum_{s=1}^{S} \sigma_{is} R_s^S,\\ \mathbf{n}\times\mathbf{v} &= 0.\end{aligned} \tag{26}$$

on the reacting boundary.[3] For the wafer surface temperature we have

$$T = T_s.$$

[2] See for instance `http://en.wikipedia.org/wiki/Silicon`

[3] The outer product of two vectors $\mathbf{u}$ and $\mathbf{v}$ is defined as

$$\mathbf{u}\times\mathbf{v} = (u_2v_3 - u_3v_2)\mathbf{e}_{(1)} + (u_3v_1 - u_1v_3)\mathbf{e}_{(2)} + (u_1v_2 - u_2v_1)\mathbf{e}_{(3)},$$

with $\mathbf{e}_{(\alpha)}$ the unit vector in the x_α direction. The outer product is anti symmetric, i.e., $\mathbf{u}\times\mathbf{v} = -\mathbf{v}\times\mathbf{u}$.

Surface Reaction	Sticking coefficient
Si (g) $\rightarrow$ Si (s)	1
SiH $\rightarrow$ Si (s) + H	1
$SiH_2 \rightarrow$ Si (s) + H_2	1
$SiH_3 \rightarrow$ Si (s) + H_2 + H	1
$SiH_4 \rightarrow$ Si (s) + $2H_2$	$0.0537e^{\frac{-9400}{T_s}}$
Si_2 (g) $\rightarrow$ 2Si (s)	1
$Si_2H_2 \rightarrow$ 2Si (s) + H_2	1
$Si_2H_3 \rightarrow$ 2Si (s) + H_2 + H	1
$H_2SiSiH_2 \rightarrow$ 2Si (s) + $2H_2$	1
$H_3SiSiH \rightarrow$ 2Si (s) + $2H_2$	1
$Si_2H_5 \rightarrow$ 2Si (s) + $2H_2$ + H	1
$Si_2H_6 \rightarrow$ 2Si (s) + $3H_2$	$0.537e^{\frac{-9400}{T_s}}$
Si_3 (g) $\rightarrow$ 3Si (s)	1
$Si_3H_8 \rightarrow$ 3Si (s) + $4H_2$	0

Table 5: Surface reactions for the silicon containing species in the gas mixture and their sticking coefficients

On the wafer surface the net mass production of species i must be equal to the normal direction of the total mass flux of species i. Since the total mass flux of species i is given by

$$\rho\omega_i\mathbf{v} + \mathbf{j}_i,$$

we have on the wafer surface the boundary condition

$$\mathbf{n} \cdot (\rho\omega_i\mathbf{v} + \mathbf{j}_i) = m_i \sum_{s=1}^{S} \sigma_{is} R_s^S. \tag{27}$$

By introducing the mass flux of species i deposited on cell face s as

$$F_{\text{wall}} = m_i \sum_{s=1}^{S} \sigma_{is} R_s^S, \tag{28}$$

(27) can be written as

$$\mathbf{n} \cdot (\rho\omega_i\mathbf{v} + \mathbf{j}_i) = F_{\text{wall}}. \tag{29}$$

4.2 Discretization of the Reacting Surface Boundary Condition for the Species Equations

The way of discretizing as done in this section is taken from [10]. We have to remark that inclusion of surface chemistry can be discretized in various manners. However, we prefer it to be discretized in a positivity conserving way.

The general form of the species equation (8) is

$$\frac{\partial(r\rho\phi)}{\partial t} = -\nabla\cdot(r^\alpha\rho v\phi) + \nabla\cdot(r^\alpha\Gamma_\phi\nabla\phi) + r^\alpha S_\phi, \tag{30}$$

whereby

$$\phi = \omega_i, \quad \Gamma_\phi = \rho\mathbb{D}_i' \quad \text{and} \quad S_\phi = m_i\sum_{k=1}^{K}\nu_{ik}R_k^g. \tag{31}$$

Note that for $\alpha = 1$ Equation (30) is in axisymmetric form and by taking $\alpha = 0$ it is in Cartesian coordinates. Next, we will compute the volume integral over the control volume surrounding the grid point P, see Figure 1.

Grid point P has four neighbors, indicated by N(orth), S(outh), E(ast) and W(est), and the corresponding walls are indicated by n, s, e and w. The south wall is the reacting surface, automatically implying that S is a virtual point. For the sake of clarity, we write in the remainder of this section

$$\mathbf{v} = \begin{bmatrix} u \\ v \end{bmatrix}, \tag{32}$$

where u is the velocity component in r-direction and v the velocity component in z-direction.

Integrating Equation (30) over the control volume $\Delta r\Delta z$ surrounding P gives

$$\begin{aligned}\iint_{\Delta r\Delta z}\frac{\partial(r^\alpha\rho\phi)}{\partial t}\,dr\,dz = \\ \iint_{\Delta r\Delta z}\left(-\nabla_{r,z}\cdot(r^\alpha\rho v\phi) + \nabla_{r,z}\cdot(r^\alpha\Gamma_\phi\nabla_{r,z}\phi) + r^\alpha S_\phi\right)\,dr\,dz.\end{aligned} \tag{33}$$

By using the Gauß theorem we may write

$$\begin{aligned}\iint_{\Delta r\Delta z}\frac{\partial(r^\alpha\rho\phi)}{\partial t}\,dr\,dz = -\int_n r^\alpha\rho v\phi\,dr + \int_s r^\alpha\rho v\phi\,dr - \int_e r^\alpha\rho u\phi\,dz + \int_w r^\alpha\rho u\phi\,dz + \\ \int_n r^\alpha\Gamma_\phi\frac{\partial\phi}{\partial z}\,dr - \int_s r^\alpha\Gamma_\phi\frac{\partial\phi}{\partial z}\,dr + \int_e r^\alpha\Gamma_\phi\frac{\partial\phi}{\partial r}\,dz - \int_w r^\alpha\Gamma_\phi\frac{\partial\phi}{\partial r}\,dz + \\ \iint_{\Delta r\Delta z} r^\alpha S_\phi\,dr\,dz.\end{aligned} \tag{34}$$

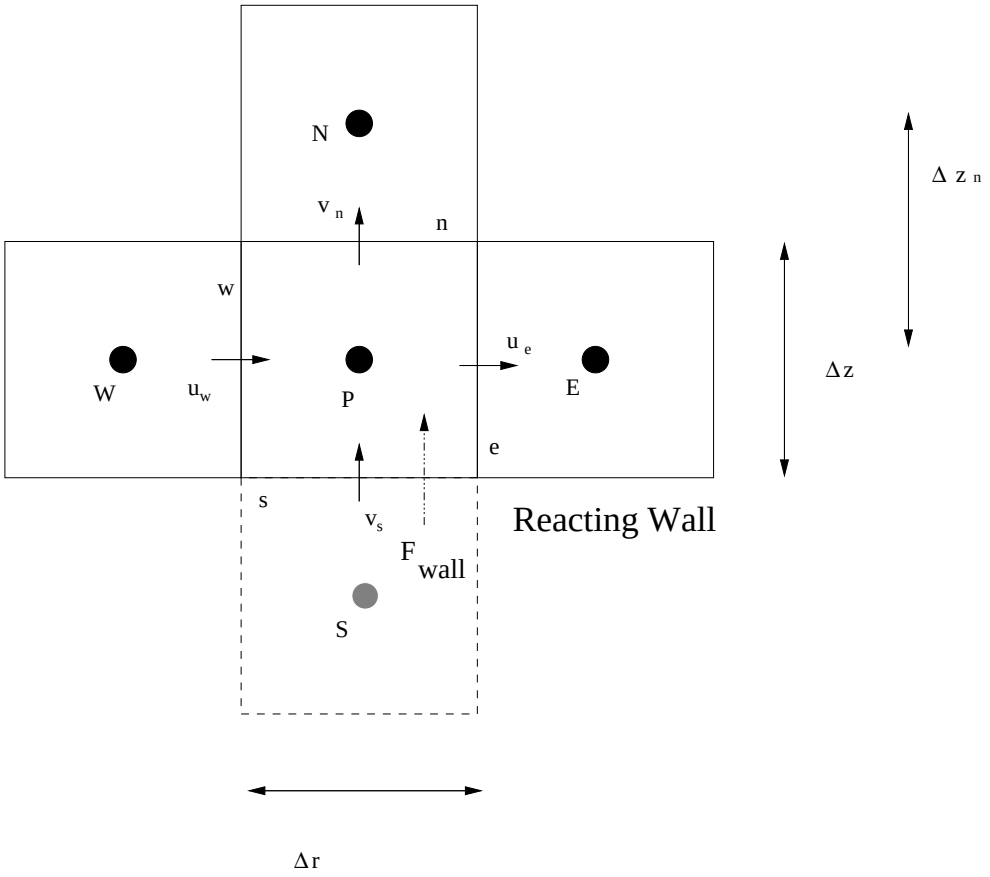

Figure 1: Reacting surface boundary condition

The remaining integrals are approximated as

$$\frac{d(r_P^\alpha \rho_P \phi_P)}{dt}\Delta r\Delta z = -r_n^\alpha \rho_n v_n \phi_n \Delta r + r_s^\alpha \rho_s v_s \phi_s \Delta r - r_e^\alpha \rho_e u_e \phi_e \Delta z + r_w^\alpha \rho_w u_w \phi_w \Delta z + r_n^\alpha \Gamma_{\phi,n} \left.\frac{\partial \phi}{\partial z}\right|_n \Delta r - r_s^\alpha \Gamma_{\phi,s} \left.\frac{\partial \phi}{\partial z}\right|_s \Delta r + r_e^\alpha \Gamma_{\phi,e} \left.\frac{\partial \phi}{\partial r}\right|_e \Delta z - r_w^\alpha \Gamma_{\phi,w} \left.\frac{\partial \phi}{\partial r}\right|_w \Delta z + r_p^\alpha S_{\phi,P} \Delta r \Delta z. \tag{35}$$

Recall that on the south cell face we imposed that the total mass transport flux in the outward normal direction should be equal to the mass flux F_{wall}, which is the mass flux due to deposition on the wafer (28), i.e.,

$$\mathbf{n} \cdot \left(\rho_s \phi_s v_s + \Gamma_{\phi,s} \frac{\partial \phi}{\partial z}|_s \right) = F_{\text{wall}}. \tag{36}$$

Since near the wafer mass transport is mainly by diffusion and not by advection, see [5], (36) reduces to

$$\Gamma_{\phi,s} \frac{\partial \phi}{\partial z}|_s = F_{\text{wall}}. \tag{37}$$

The mass diffusion flux can be approximated as

$$\Gamma_{\phi,s} \frac{\partial \phi}{\partial z}|_s = \frac{2\mathbb{D}}{\Delta z}(\phi_P - \phi_{\text{wall}}), \tag{38}$$

where ϕ_{wall} is the species mass fraction on the reacting wall. For now, the mass fraction ϕ_{wall} is unknown. However, we are not interested in computing the mass diffusion flux, but in F_{wall}, which has to be computed using ϕ_{wall}. According to (23), for the type of surface reactions assumed in the present report, the molar reactive surface flux is linearly proportional to the species molar concentration at the wafer. Consequently, the reactive surface mass flux is linearly proportional to the species mass fraction, and is denoted as

$$F_{\text{wall}} = \mathcal{R}^S \phi_{\text{wall}}, \tag{39}$$

with $\mathcal{R}^S \geq 0$. Then, ϕ_{wall} can be computed from (37) - (39) as

$$\phi_{\text{wall}} = \frac{\phi_P}{1 + \frac{\Delta z \mathcal{R}^S}{2\mathcal{D}}}. \tag{40}$$

Remark that ϕ_{wall} is positive when ϕ_P is positive, and $\phi_{\text{wall}} \leq 1$ as long as $\phi_P \leq 1$.

Finally, the semi discretization in a control volume near the reacting surface becomes

$$\frac{d(r_P^\alpha \rho_P \phi_P)}{dt}\Delta r\Delta z = -r_n^\alpha \rho_n v_n \phi_n \Delta r - r_e^\alpha \rho_e u_e \phi_e \Delta z + r_w^\alpha \rho_w u_w \phi_w \Delta z + r_n^\alpha \Gamma_{\phi,n} \left.\frac{\partial \phi}{\partial z}\right|_n \Delta r + r_e^\alpha \Gamma_{\phi,e} \left.\frac{\partial \phi}{\partial r}\right|_e \Delta z - r_w^\alpha \Gamma_{\phi,w} \left.\frac{\partial \phi}{\partial r}\right|_w \Delta z + r_p^\alpha S_{\phi,P} \Delta r \Delta z + r_s^\alpha F_{\text{wall}} \Delta r, \tag{41}$$

where F_{wall} is computed implicitly from ϕ_P as in (39) with ϕ_{wall} as in (40).

Note that the approach for spatial discretization of the reacting boundary in this paper is conserves positivity, unlike the approach given in [5].

5 Numerical Methods

Suitable numerical methods for solving the stiff, nonlinearly coupled system of species equations should be

1. Stable with respect to the integration of the stiff reaction terms,
2. Positive with respect to spatial and time integration, and the iterative solvers,
3. Efficient.

In [12] a number of time integration methods has been selected in order to solve a simplified CVD system. These methods satisfy the first two properties mentioned above. This so-called simplified CVD system contains

1. a gas phase chemistry model consisting of 5 gas phase reactions,
2. no surface reactions.

This simplified CVD system does not represent a (realistic) practical process, but a simplified version that represents its computational problems only. In this paper we consider the same collection of time integration methods as in [12], and again compare them in terms of efficiency. Following [12], for spatial discretization the hybrid scheme has been used. Recall that the hybrid scheme uses second order central differencing and introduces locally first order upwinding to avoid numerical instabilities. For the exact finite volume discretization we refer to [11].

In this section we first describe the (variable) time step controller that we used in our code. This controller is based on a local truncation error estimation, as is custom in MOL solvers in the ODE field. Subsequently, the time integration methods used in [11] are briefly described.

5.1 Variable Time Step Controller

We briefly explain the variable time stepping algorithm as it is implemented in our code. Consider an attempted step from t_n to $t_{n+1} = t_n + \tau_n$ with time step size τ_n that is performed with an p^{th} order time integration method. Suppose an estimate D_n of order $\hat{p}$ of the norm of the local truncation error is available. Then, if $D_n < Tol$ this step τ_n is accepted, whereas if $D_n > Tol$ the step is rejected and redone with time step size $\frac{1}{2}\tau_n$. If $D_n < Tol$, then the new step size is computed as

$$\tau_{\text{new}} = r \cdot \tau, \quad r = \left(\frac{Tol}{D_n}\right)^{\frac{1}{\hat{p}+1}}. \tag{42}$$

Because estimates are used and additional control on decrease and increase of step sizes is desirable. In the ODE field it is customary to implement the following new (trial) time step

$$\tau_{\text{new}} = \min(r_{max}, \max(r_{min}, \vartheta r)) \cdot \tau, \quad r = \left(\frac{Tol}{D_n}\right)^{\frac{1}{\hat{p}+1}}. \tag{43}$$

In (43) r_{max} and r_{min} are the maximal and minimal growth factor, respectively, and $\vartheta < 1$ serves to make the estimate conservative so as to avoid multiple rejections.

Besides the estimation of the new time step the controller in our code also checks whether (i) the solution is positive, and (ii) Newton's method is converged. In the case of Newton divergence the time step size is halved and the time step redone. In the case of negative species, we first check whether these negative mass fractions are due to rounding errors, and if not, the time step is redone with a halved time step size.

For each time integration method discussed in this section, a local error estimation, needed for the time step controller, will be given.

5.2 Euler Backward

The well known Euler Backward method is defined as

$$w_{n+1} = w_n + \tau F(t_n, w_{n+1}). \tag{44}$$

It is generally known that this method is unconditionally stable, and even L stable. In [12] it has been shown that Euler Backward is also unconditionally positive, under the assumption that the resulting nonlinear systems are solved exactly. In practice, exact solutions of nonlinear systems cannot be found. This means that Euler Backward is not unconditionally positive in practice.

The local truncation error of the Euler Backward method

$$\delta_n = -\frac{1}{2}\tau^2 w''(t_n) + \mathcal{O}(\tau^3), \tag{45}$$

can be estimated as

$$d_n = -\frac{1}{2}\left(w_{n+1} - w_n - \tau F(t_n, w_n)\right). \tag{46}$$

See also [4].

5.3 Rosenbrock Methods

In [12] the second order Rosenbrock scheme

$$\begin{aligned} w_{n+1} &= w_n + \frac{3}{2}k_1 + \frac{1}{2}k_2, \\ k_1 &= \tau F(w_n) + \gamma\tau J_F k_1, \\ k_2 &= \tau F(w_n + k_1) - 2k_1 + \gamma\tau J_F k_2, \end{aligned} \tag{47}$$

where J_F is the Jacobian of F with respect to w, has been implemented. This scheme has the property that $R(z) \geq 0$ for all negative real z. For diffusion reaction problems positivity is then assured. In the case advection is added, this method still performs well with respect to positivity. We refer to [12] for more information.

The local error estimation for the Rosenbrock method can be taken equal to the Euler Backward error estimation.

5.4 Backward Differentiation Formulas (BDF)

The k-step BDF methods are implicit, of order k and defined as

$$\sum_{j=0}^{k} \alpha_j w_{n+j} = \tau F(t_{n+k}, w_{n+k}), \quad n = 0, 1, \ldots, \tag{48}$$

which uses the k past values $w_n, \ldots, w_{n+k-1}$ to compute w_{n+k}. Remark that the most advanced level is t_{n+k} instead of t_{n+1}. The 1-step BDF method is Backward Euler. The 2-step method is

$$\frac{3}{2}w_{n+2} - 2w_{n+1} + \frac{1}{2}w_n = \tau F(t_{n+2}, w_{n+2}), \tag{49}$$

and the three step BDF is given by

$$\frac{11}{6}w_{n+3} - 3w_{n+2} + \frac{3}{2}w_{n+1} - \frac{1}{3}w_n = \tau F(t_{n+3}, w_{n+3}). \tag{50}$$

We implemented the 2-step BDF scheme, whereof some properties are discussed below.

Under the assumption that w_{n+1} is computed from a suitable starting procedure that is positive, the 2-step BDF method is positive under the restriction $\alpha\tau \leq \frac{1}{2}$, where $\alpha > 0$ and $\alpha\tau < 1$ such that

$$v + \tau F(t, v) \geq 0 \quad \text{for all} \quad t \geq 0, v \geq 0. \tag{51}$$

For the BDF-2 scheme the local error estimation is as follows. Introduce the ratio $r = \frac{\tau_n}{\tau_{n-1}}$, where τ_n is defined as above, e.g., $\tau_n = t_{n+1} - t_n$. The second order BDF-2 scheme can be rewritten in the form with the ratio r as

$$w_{n+2} - \frac{(1+r^2)}{1+2r}w_{n+1} + \frac{r^2}{1+2r}w_n = \frac{1+r}{1+2r}\tau F(t_{n+2}, w_{n+2}). \tag{52}$$

A first order estimator, see [4], is

$$d_n = \frac{r}{1+r}\left(w_{n+1} - (1+r)w_n + rw_{n-1}\right). \tag{53}$$

A second order estimator, see [4], is

$$d_n = \frac{1+r}{1+2r}\left(w_{n+1} + (r^2-1)w_n - r^2 w_{n-1} - (1+r)\tau_n F(t_n, w_n)\right). \tag{54}$$

We remark that in the first time step, where BDF-1 is used, the local error is estimated by

$$d_0 = \frac{1}{2}\left(w_1 - w_0 - \tau_0 F(t_0, w_0)\right). \tag{55}$$

IMEX Runge-Kutta Chebyshev Methods

The second order Runge-Kutta Chebyshev method is given as

$$\begin{aligned} w_{n0} &= w_n, \\ w_{n1} &= w_n + \tilde{\mu}_1 \tau F(t_n + c_0\tau, w_{n0}), \\ w_{nj} &= (1-\mu_j-\nu_j)w_n + \mu_j w_{n,j-1} + \nu_j w_{n,j-2} + \quad j = 1,\ldots,s \\ &\quad +\tilde{\mu}_1\tau F(t_n + c_{j-1}\tau, w_{n,j-1}) + \tilde{\gamma}_j \tau F(t_n + c_0\tau, w_{n0}), \\ w_{n+1} &= w_{ns}. \end{aligned} \tag{56}$$

The coefficients $\tilde{\mu}_1, \mu_j, \nu_j, \tilde{\mu}_j$ and $\tilde{\gamma}_j$ are available in analytical form for $s \geq 2$:

$$\tilde{\mu}_1 = b_1\omega_1 \quad \text{and for} \quad j = 2,\ldots,s, \tag{57}$$

$$\mu_j = \frac{2b_j\omega_0}{b_{j-1}}, \quad \nu_j = \frac{-b_j}{b_{j-2}}, \quad \tilde{\mu}_j = \frac{2b_j\omega_1}{b_{j-1}}, \quad \tilde{\gamma}_j = -a_{j-1}\tilde{\mu}_j, \tag{58}$$

where

$$b_0 = b_2, \quad b_1 = \frac{1}{\omega_0}, \quad b_j = \frac{T_j''(\omega_0)}{(T_j'(\omega_0))^2}, \quad j = 2,\ldots,s, \tag{59}$$

with

$$\omega_0 = 1 + \frac{\varepsilon}{s^2}, \quad \text{and} \quad \omega_1 = \frac{T_s'(\omega_0)}{T_s''(\omega_0)}. \tag{60}$$

Furthermore,

$$c_0 = 0, c_1 = c_2, c_j = \frac{T_s'(\omega_0)}{T_s''(\omega_0)}\frac{T_j''(\omega_0)}{T_j'(\omega_0)}, c_s = 1, \tag{61}$$

and,

$$a_j = 1 - b_j T_j(\omega_0). \tag{62}$$

In (59) - (62) $T_j(x)$ are the Chebyshev polynomials of the first kind satisfying the recursion

$$T_j(x) = 2xT_{j-1}(x) - T_{j-2}(x), \quad j = 2,\ldots,s, \tag{63}$$

with $T_0(x) = 1$ and $T_1(x) = x$. Furthermore, in (60) ε is a free parameter. In Figure 2 its stability region is given. The parameter $\beta(s)$ moves to $-\infty$ when the number of stages s increases. For ε small, by which we mean $\frac{\varepsilon}{s^2} \ll 1$, the stability bound $\beta(s)$ satisfies

$$\beta(s) \approx \frac{2}{3}\left(s^2 - 1\right)\left(1 - \frac{2}{15}\varepsilon\right). \tag{64}$$

The IMEX extension of (56) is as follows. Suppose we have an ODE system $w'(t) = F(t, w(t))$, where $F(t, w(t))$ can be split as

$$F(t, w(t)) = F_E(t, w(t)) + F_I(t, w(t)). \tag{65}$$

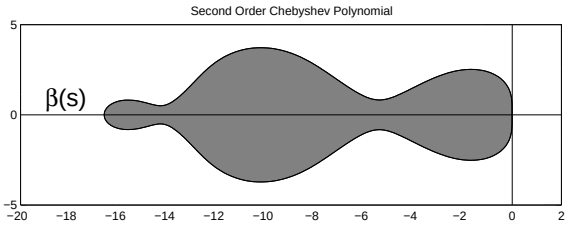

Figure 2: Stability region of (56) for $s = 5$.

In (65) the term $F_I(t, w(t))$ is the part of F which is (supposed to be) too stiff to be integrated by an explicit Runge-Kutta Chebyshev method. Obviously, the term $F_E(t, w(t))$ is the moderate stiff part of F that can be integrated in an explicit manner using RKC methods. The first stage of (56) becomes in the IMEX-RKC scheme

$$w_{n1} = w_n + \tilde{\mu}_1 \tau F_E(t_n + c_0\tau, w_{n0}) + \tilde{\mu}_1 \tau F_I(t_n + c_1\tau, w_{n1}), \tag{66}$$

with $\tilde{\mu}_1$ as defined before. Note that the highly stiff part of F is treated implicitly. The other $(s-1)$ subsequent stages of (56) will be modified in a similar way, such that in each of the remaining $s-1$ stages the solution of a system of nonlinear algebraic equations

$$w_{nj} - \tilde{\mu}_1 \tau F_I(t_n + c_j\tau, w_{nj}) = v_j, \tag{67}$$

with v_j a given vector, is required.

With respect to stability of this IMEX extension of (56) we remark that the implicit part is unconditionally stable, whereas the stability condition for the explicit part remains unchanged. For more background we refer to [13, 14].

The local error estimation for the IMEX -Runge-Kutta-Chebyshev methods is the same as for the explicit Runge-Kutta-Chebyshev schemes, see [14]. The asymptotically correct estimate of the local error is

$$d_n = \frac{1}{15}\left[12(w_n - w_{n+1}) + 6\tau_n(F(t_n, w_n) + F(t_{n+1}, w_{n+1}))\right], \tag{68}$$

which is taken from [9].

The code is also equipped with a number of stages selector. This procedure returns the number of stages s, depending on the time step size τ, and the stability condition arising from von Neumann stability analysis to ensure stable explicit RKC integration for advection and diffusion. Following [14], this procedure can test on stability for diffusion only, which will be called the 'on the fly condition', or, there can be tested on the full advection and diffusion stability conditions. Detailed information on von Neumann stability analysis of the explicit integration of advection and diffusion can, for instance, be found in [12, 14, 15].

6 Simulation on a Simple Geometry

In this section we consider the benchmark problem as defined in Sections 2 to 4 on a simple geometry. The reactor is a square, 10 by 10 cm., with the pressure equal to the

atmospheric pressure. At the top of the reactor is the inflow boundary, whereas at the bottom the outflow boundary is situated. The other walls are adiabatic solid walls, and there is no reacting surface within this reactor configuration. The velocity field depends on the z coordinate only, and is constant, i.e., $v_z = -0.1\ [\frac{m}{s}]$. Furthermore, the density field is also taken constant, i.e., $\rho = 1$ over the whole (computational) domain. The temperature depends linearly on the spatial variable z as

$$T(z) = 1000 - 3000z. \tag{69}$$

See also Figure 3. Remark that the solution of this problem depends only on the z-coordinate.

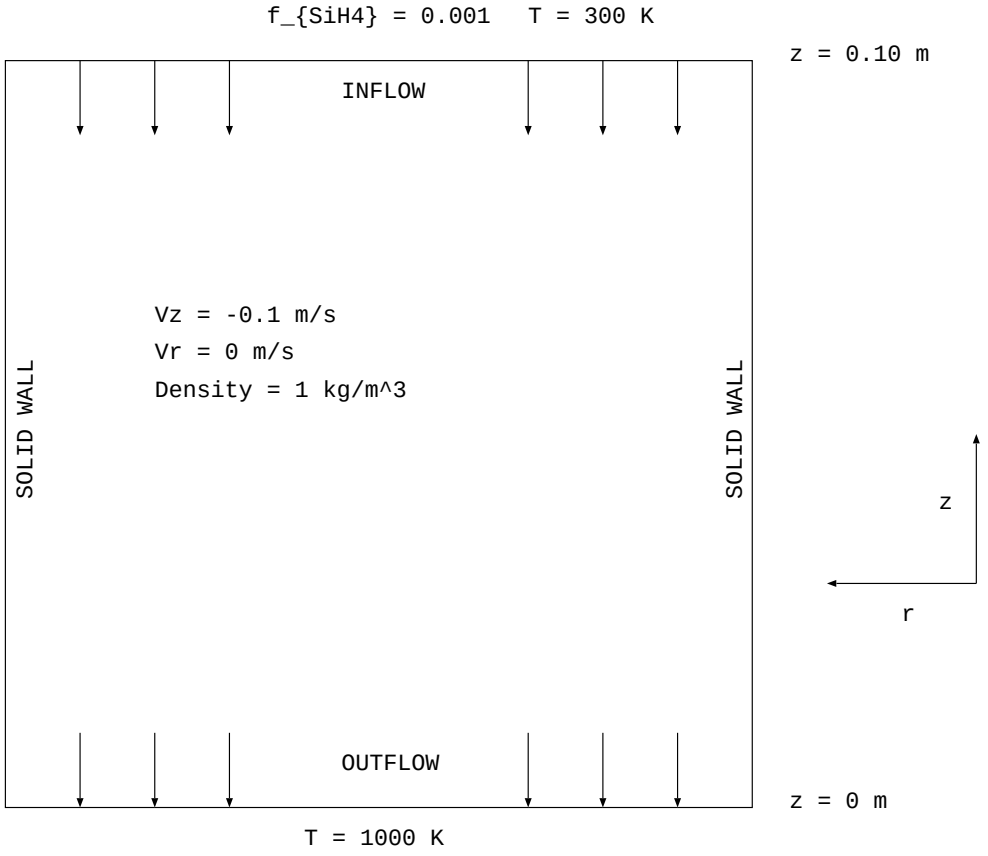

Figure 3: Geometry and parameter values of the simplified problem

It appears that for the simulation from the initial state, which is equal to a zero concentration profile for all species on the domain, till steady state can give 'poor' Newton convergence. We mean that from the moment that the 'fast' reactions come into play, the condition number of the Jacobian grows very fast, and the number of Linesearch calls within the Newton iteration becomes very large. Often, when linesearch is needed to enforce global convergence, the Newton iteration will diverge.

In Table 6 the integration statistics are given for the benchmark problem on the simplified geometry as described above. Spatial discretization is done by means of the hybrid scheme, and for time integration Euler Backward is used. If we do the same simulation without the last gas phase reaction, i.e.,

$$H_3SiSiH \rightleftharpoons H_2SiSiH_2, \tag{70}$$

the integration statistics show that the performance is much better, see Table 6. If we also look at the development of the condition number of the Jacobian with respect to time, then we see that in the case of 25 reactions it is two to three orders of magnitude smaller than before. Of course, for the quality of the Newton updates this is more convenient. In Figure 4 the condition numbers of to the Jacobian matrix belonging to the Euler Backward time discretization are given as a function of the time step for both the 25 and 26 reaction system. The condition numbers in Figure 4 are estimations of the condition number in the infinity norm, i.e.,

$$\|B\|_\infty = \max_{1\leq j\leq m} \sum_{k=1}^{m} |b_{jk}|, \quad \text{where} \quad B = (b_{jk}). \tag{71}$$

There estimations are obtained with routines from the LAPACK package, see [1]. The irregular behavior of the condition number is partly due to the norm used to measure and partly due to the time step adjustments to enforce Newton convergence and/or positivity. It appears that Newton convergence and/or positivity is easier satisfied when the last reaction is removed from the system, as can be seen in the magnitude and the more regular behavior of the condition number in time.

In order to achieve this also for the reaction system of 26 reactions we apply diagonal scaling to the linear systems within the Newton solver. We then obtain the results as given in Table 7. For the similar system without the last reaction, we obtain no difference in the integration statistics if diagonal scaling is applied.

In Figure 5 the largest condition number per time step, with and without diagonal scaling, is given for the simulation on a 5×5 grid with Euler Backward time discretization.

We conclude that reaction (70) is responsible for higher condition number of the Jacobian belonging to the nonlinear systems of the Euler Backward discretization. Application of diagonal scaling takes care of a two order of magnitude drop of the condition number. Our experiments show that this modification to the direct solver gives a better performance in terms of efficiency.

6.1 Higher Order TIM for Solving the Benchmark on the Simple Geometry

In the previous part we concluded that application of diagonal scaling to the linear systems for the Newton update, where Euler Backward has been used to integrate in time, increases the performance. In the following section we present similar results for the time integration methods presented in Section 5.

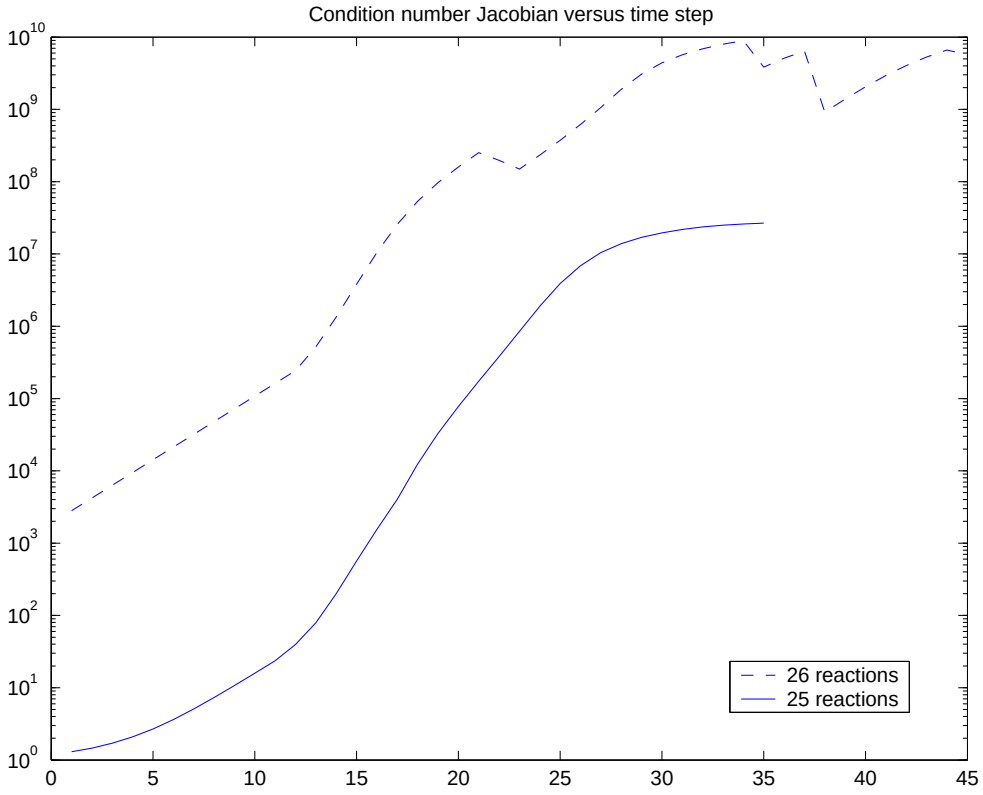

Figure 4: Condition number of the Jacobian belonging to Euler Backward time discretization versus the time step. Spatial grid is 5×5.

	4×4 grid		5×5 grid		10×10 grid	
# reactions	25	26	25	26	25	26
$\#F$	128	193	136	443	153	739
$\#F'$	54	67	57	94	62	125
# Linesearch	4	48	9	249	18	449
# Newton iters	54	67	57	94	62	125
# Rej. time steps	0	2	0	10	1	15

Table 6: Integration statistics without diagonal scaling

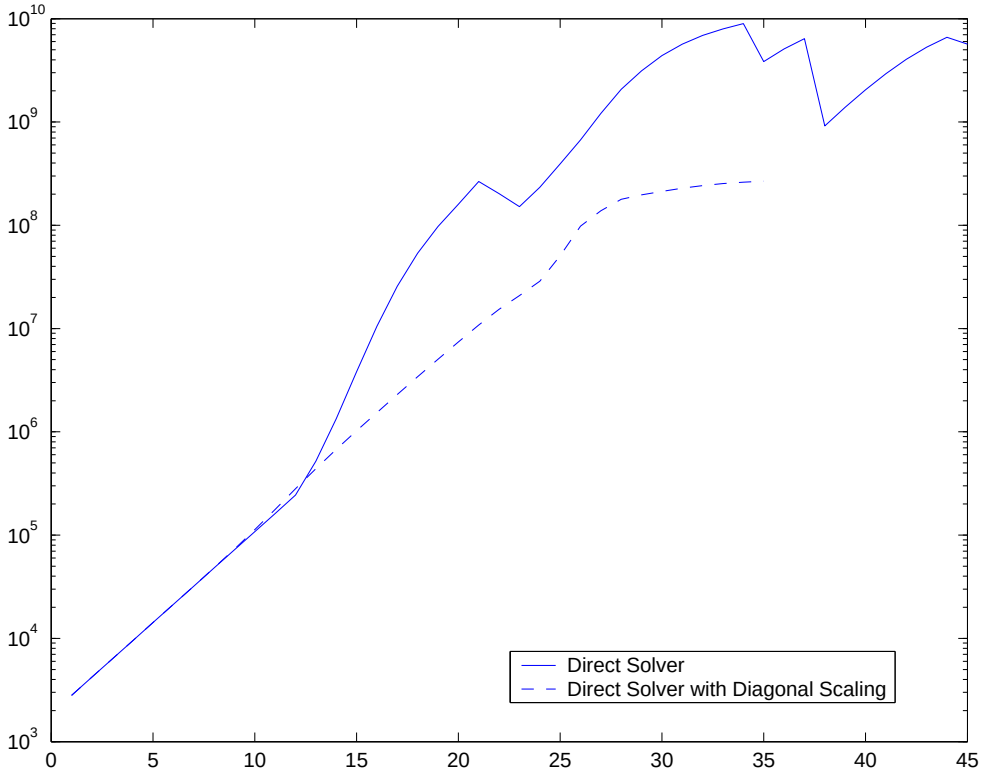

Figure 5: Maximum condition number of Jacobian with and without Jacobi preconditioning. Time discretization is Euler Backward. Spatial grid is 5×5.

	4×4 grid		5×5 grid		10×10 grid	
# reactions	25	26	25	26	25	26
$\#F$	128	131	136	131	153	129
$\#F'$	54	59	57	58	62	58
# Linesearch	4	2	9	3	18	3
# Newton iters	54	59	57	58	62	58
# Rej. time steps	0	0	0	0	1	0

Table 7: Integration statistics with diagonal scaling

6.1.1 Rosenbrock

The ROS2 method has been implemented with the time step controller as presented in Section 5. In (43) the following values have been taken

$$r_{max} = 1.5, \quad r_{min} = 0.7, \quad \text{and}, \quad \theta = 0.9. \tag{72}$$

We see in Table 8 and 9 that preconditioning the linear systems does not increase the performance. The main difference with Euler Backward and BDF is that the Newton iteration performs better with the scaled linear systems, in particular in the second Newton iterate and further. Since ROS2 is a linearized scheme it has no benefit from the diagonal scaling.

	4×4 grid		5×5 grid		10×10 grid	
# reactions	25	26	25	26	25	26
$\#F$	176	176	188	184	244	240
$\#F'$	44	44	47	46	61	60
# Rej. time steps	0	0	0	0	0	0

Table 8: Integration statistics ROS2 without diagonal scaling

	4×4 grid		5×5 grid		10×10 grid	
# reactions	25	26	25	26	25	26
$\#F$	176	176	188	184	244	240
$\#F'$	44	44	47	46	61	60
# Rej. time steps	0	0	0	0	0	0

Table 9: Integration statistics ROS2 with diagonal scaling

6.1.2 BDF2

The BDF2 method has been implemented with the time step controller as presented in Section 5. In (43) identical values have been taken for r_{max}, r_{min} and ϑ.

We see in Table 10 and 11 that preconditioning the linear system in the Newton update increases the performance.

6.1.3 IMEX RKC

The IMEX RKC method has been implemented with the time step controller as presented in Section 5. In (43) identical values have been taken for r_{max}, r_{min} and ϑ. Furthermore, we remark that from the point of view of efficiency for the nonlinear systems the

	4×4 grid		5×5 grid		10×10 grid	
# reactions	25	26	25	26	25	26
$\#F$	183	312	193	297	nc	300
$\#F'$	62	87	65	83	nc	92
# Linesearch	1	86	5	71	nc	51
# Newton iters	62	87	65	83	nc	92
# Rej. time steps	0	4	0	5	nc	7

Table 10: Integration statistics BDF2 without diagonal scaling. NC means that the simulation did not converge to a steady state solution.

	4×4 grid		5×5 grid		10×10 grid	
# reactions	25	26	25	26	25	26
$\#F$	183	191	193	190	235	229
$\#F'$	62	68	65	67	79	80
# Linesearch	1	0	5	0	3	0
# Newton iters	62	68	65	67	79	80
# Rej. time steps	0	0	0	0	3	2

Table 11: Integration statistics BDF2 with diagonal scaling

modified Newton iteration has been used. Then, in each time step only one LU factorization of $[I - \tilde{\mu}_1 \tau F'(t, w(t))]$, where $F'(t, w(t))$ is the Jacobian of $F(t, w(t))$ with respect to $w(t)$, has to be computed. The time step controller is linked with a controller for the number of IMEX-RKC stages, as has been described in [12, 14]. With respect to the number of IMEX-RKC stages controller there are two possibilities:

1. On the fly, meaning that for the conditional stability only the diffusion part is considered,

2. Conditional stability is also tested for the advection part.

For both strategies tests have been carried out, whereof the results are presented in Table 12 up to and including Table 15. We tested on 5×5 and 10×10 spatial grids, for the damping parameters $\varepsilon = 1$ and $\varepsilon = 10$.

We observe that diagonal scaling does not influence the performance at all. An explanation is that for each Newton iteration a good estimate of the nonlinear solution is available, resulting in convergence within one Newton iteration.

7 Numerical Results

In this section we present results on the simulations of the benchmark problem of Kleijn [8]. We remark that in the CVD community the steady state solution found by Kleijn is

	5×5 grid		10×10 grid	
# reactions	25	26	25	26
$\#F$	2348 (3338)	2348 (3338)	3218 (4680)	3218 (4350)
$\#F'$	29 (36)	29 (36)	34 (50)	34 (47)
# Linesearch	0	0	0	0
# Newton iters	587 (835)	587 (835)	805 (1173)	805 (1090)
# Rej. time steps	0 (1)	0 (1)	1 (6)	1 (5)
# Acc. time steps	29 (35)	29 (35)	33 (44)	33 (42)
$s_{\max}$	51	51	56	56

Table 12: Integration statistics IMEX RKC without diagonal scaling. Damping parameter $\varepsilon = 10$. If the results for damping parameter $\varepsilon = 1$ differ from the results for $\varepsilon = 10$, then they are given between brackets. The number of stages are controlled by controlling stability for both advection and diffusion.

	5×5 grid		10×10 grid	
# reactions	25	26	25	26
$\#F$	2348 (3338)	2348 (3338)	3218 (4680)	3218 (4680)
$\#F'$	29 (36)	29 (36)	34(50)	34(50)
# Linesearch	0	0	0	0
# Newton iters	587 (835)	587 (835)	805 (1173)	805 (1173)
# Rej. time steps	0 (1)	0 (1)	1 (6)	1 (6)
# Acc. time steps	29 (35)	29 (35)	33 (44)	33 (44)
$s_{\max}$	51	51	56	56

Table 13: Integration statistics IMEX RKC with diagonal scaling. Damping parameter $\varepsilon = 10$. If the results for damping parameter $\varepsilon = 1$ differ from the results for $\varepsilon = 10$, then they are given between brackets. The number of stages are controlled by controlling stability for both advection and diffusion.

	5×5 grid		10×10 grid	
# reactions	25	26	25	26
$\#F$	3580 (15050)	3580 (15050)	5150 (12618)	5150 (18134)
$\#F'$	29 (39)	29 (39)	34 (53)	34 (51)
# Linesearch	0	0	0	0
# Newton iters	895 (3763)	95 (3763)	1288 (3158)	1288 (4536)
# Rej. time steps	0 (1)	0 (1)	1 (7)	1 (5)
# Acc. time steps	29 (38)	29 (38)	33 (46)	33 (46)
$s_{\max}$	156 (676)	156 (676)	208 (425)	208 (777)

Table 14: Integration statistics IMEX RKC without diagonal scaling. Damping parameter $\varepsilon = 10$. If the results for damping parameter $\varepsilon = 1$ differ from the results for $\varepsilon = 10$, then they are given between brackets. The number of stages are controlled by the on the fly condition.

	5×5 grid		10×10 grid	
# reactions	25	26	25	26
$\#F$	3580(15050)	3580(15050)	5150 (12618)	5150 (12614)
$\#F'$	29(39)	29(39)	34 (53)	34 (53)
# Linesearch	0	0	0	0
# Newton iters	895 (3763)	895(3763)	1288 (3158)	1288 (3157)
# Rej. time steps	0 (1)	0 (1)	1 (7)	1 (7)
# Acc. time steps	29 (38)	29 (38)	33 (46)	33 (46)
$s_{\max}$	156 (676)	156 (676)	208 (425)	208 (424)

Table 15: Integration statistics IMEX RKC with diagonal scaling. Damping parameter $\varepsilon = 10$. If the results for damping parameter $\varepsilon = 1$ differ from the results for $\varepsilon = 10$, then they are given between brackets. The number of stages are controlled by the on the fly condition.

considered to be correct. Actually, in the present simulations thermal diffusion (Soret effect) was neglected. Therefore, we compare our results with the results obtained with the code used in [8], where the experiments have been redone without thermal diffusion. Before giving the results, we first give details on the reactor and the simulation strategy itself.

7.1 Simulation strategy

In [8] a steady state solution of the problem stated in Sections 2 - 4 has been computed for approximately the same reactor configuration as presented in Section 7.2.

We perform transient simulations with the different time integration methods as presented in this paper. The transient simulations continue until 'numerical steady state' is obtained. Numerical steady state is defined as: for a certain index n holds that

$$\frac{\|y_{n+1} - y_n\|}{\|y_n\|} \leq \mathcal{O}(10^{-6}), \tag{73}$$

where y_n is the numerical solution vector of the semi-discretization

$$w'(t) = F(t, w(t)). \tag{74}$$

In (74) $F(t, w(t))$ represents the finite volume discretization of the species equations, as has been done in [11, 12]. More detailed information on the simulation strategy can be found in [12].

7.2 Reactor Configuration

The reactor configuration is given in Figure 6. As computational domain we take, because of axisymmetry, one half of the (r-z) plane. The pressure in the reactor is 1 atm $= 1.01325 \times 10^5$ Pa. From the top a gas-mixture, consisting of silane SiH_4 and helium

He, enters the reactor with a uniform temperature $T_{\text{in}} = 300$ K and a uniform velocity $u_{\text{in}} = 0.10$ $[\frac{\text{m}}{\text{s}}]$. The inlet silane mole fraction is $f_{\text{in,SiH}_4} = 0.001$, whereas the rest is helium. At a distance of 10 cm. below the inlet a susceptor with temperature $T = 1000$ K and a diameter 30 cm. is placed. Unlike the problem considered in [8] the susceptor does not rotate. Furthermore, the inner and outer side of the reactor walls are adiabatic and do not rotate.

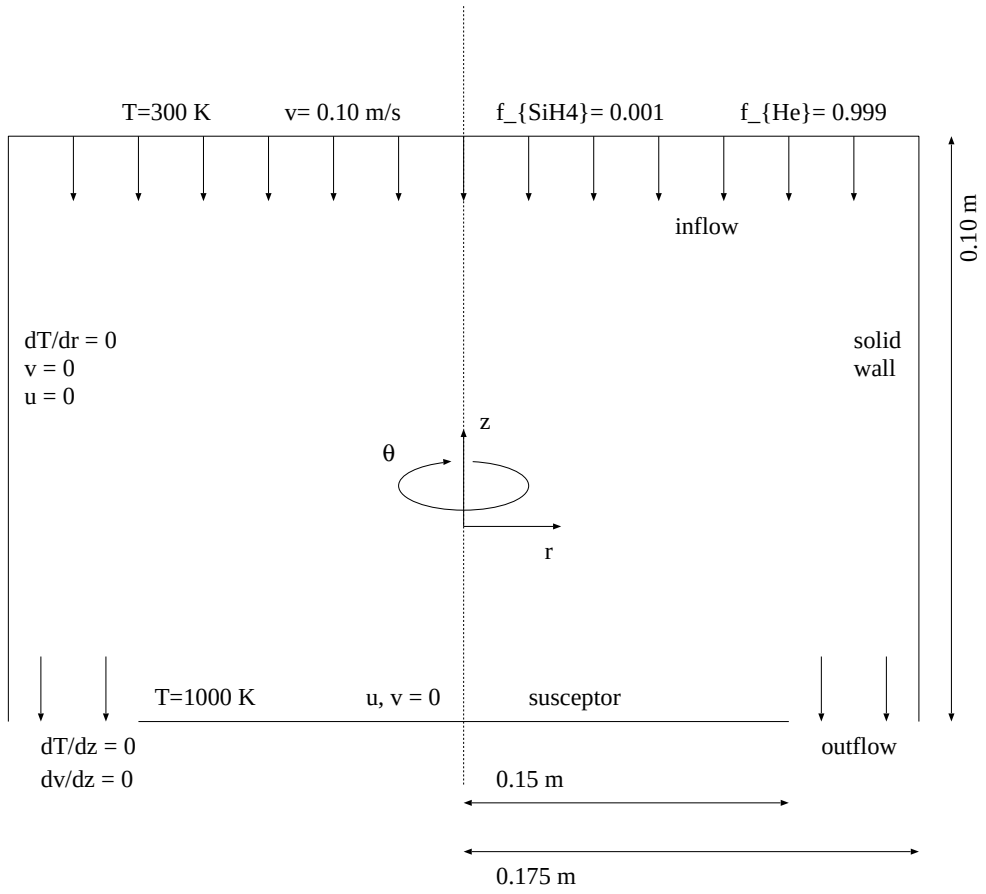

Figure 6: Reactor geometry

The velocity field, temperature field, pressure field and density field are assumed to be known. In Figure 7 the streamlines and temperature field are given for the reactor configuration as presented in this section. The streamlines are computed from the velocity fields obtained by the code of Kleijn [8].

7.3 Numerical Simulation Without Reacting Surface

In this section we present results of the transient simulations with the different time integration methods discussed in this paper. Except for the IMEX RKC method, we use, if

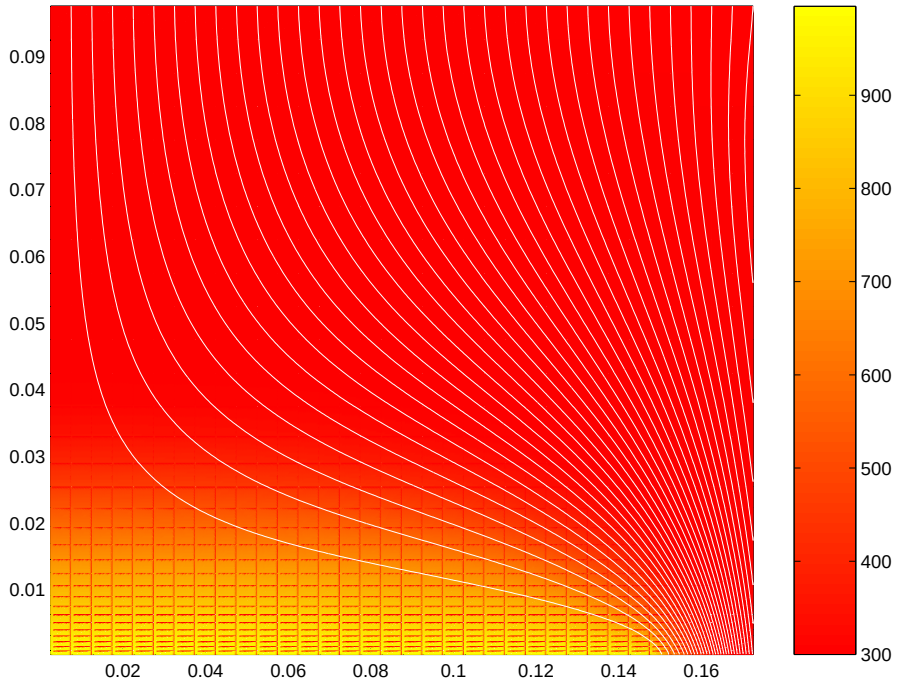

Figure 7: Streamlines and temperature field for the reactor configuration. The velocity and temperature fields are obtained by the code used in [8].

a nonlinear solver is needed, the full Newton iteration. As linear solver within the Newton iteration a direct solver with diagonal scaling is used. Without diagonal scaling the Newton updates are very poor for both the Euler Backward as the BDF-2 time discretization. See also Section 6 where the same is observed for simulations on a simple geometry. Also for the Rosenbrock time integration we observe that without preconditioning the updates in the intermediate stages are poor. In Table 16 the integration statistics are given for Euler Backward, Rosenbrock and BDF-2.

	EB	ROS2	BDF-2
$\#F$	192	551	510
$\#F'$	74	191	241
# Linesearch	28	0	42
# Newton iters	74	0	241
# Rej. time steps	0	22	14
# Acc. time steps	37	169	92
CPU Time	5500	12200	23280

Table 16: Integration statistics for Euler Backward, Rosenbrock and BDF-2.

For the integration statistics of IMEX RKC we refer to Table 17. It is remarkable that the number of rejected time steps is quite high. These rejections are due to negative species concentrations when computing to chemical steady state and the conditional positivity of IMEX RKC. When the solution is nearly steady state the time step controller returns larger estimates for the succeeding time step, and consequently a larger number of stages have to be computed, that violates the 'unknown' positivity condition.

stability condition	on the fly		full adv.-diff.	
	$\varepsilon = 1$	$\varepsilon = 10$	$\varepsilon = 1$	$\varepsilon = 10$
$\#F$	71306	52714	57568	43278
$\#F'$	450	247	402	246
# Linesearch	0	0	0	0
# Newton iters	18016	13219	14452	10884
# Rej. time steps	156	81	120	49
# Acc. time steps	294	166	282	197
$s_{\max}$	92	126	55	55
CPU Time	13800	8600	13700	9700

Table 17: Integration statistics IMEX RKC with damping parameter $\varepsilon = 1$ and $\varepsilon = 10$. The number of stages are controlled by the on the fly condition and the full advection-diffusion stability condition.

For some selected species, to be precise the species as in Figure 6 of [8], the steady state axial mass fraction profiles are presented in Figure 8. It can be seen from Figure 8 that our steady state solution agrees well with the solution found in [8].

7.4 Numerical Simulation Including Reacting Surface

The simulations of the benchmark problem with reacting surface are done for the reactor configuration as presented in Section 7.2. The reacting surface is situated near the outflow, at the bottom of the reactor (In Figure 6 the reacting surface is called susceptor). The code of Section 7.3 has to be extended with a routine that returns an update of the vector of boundary conditions in every time step and/or Newton iteration. The reacting surface mass fluxes are computed in the positivity conserving way described in Section 4.2.

From the experiments we observed that inclusion of a reacting surface increases the total computational costs. In the case of added surface chemistry, more 'fast' components are actually added to the system. To correctly follow the transient solution smaller time steps are needed. The integration statistics of our experiments are given in Table 18. For both IMEX RKC schemes holds that for the damping parameter $\varepsilon = 10$ the maximum number of stages is equal to 52, and for $\varepsilon = 1$ equal to 50.

Note that the total computational costs for IMEX RKC are in this experiment somewhat smaller, but the difference between both is for CPU times in the region of noise[4].

In order to compare our steady state solution with the one obtained with the computer code of [8], we give mass fraction profiles for some selected species along the symmetry axis (as a function of the height of the reactor), see Figure 9. Furthermore, we measured in steady state a deposition rate of solid silicon of 2.43 $\frac{\text{nm}}{\text{s}}$, against a deposition rate of 2.49 $\frac{\text{nm}}{\text{s}}$ obtained with the code of [8]. Again, we conclude that our steady state solution agrees well with the one found in [8].

Number of	EB	ROS2	BDF-2	IMEX RKC(fly)	IMEX RKC(full)
F	491	2114	3697	65704 (77480)	66639 (77424)
F'	231	802	1402	588 (1018)	589 (1018)
Linesearch	68	0	24	0	0
Newton iters	231	0	1402	16747(19500)	16770 (19540)
Rej. time steps	5	292	489	210 (370)	210 (370)
Acc. time steps	94	510	893	378 (648)	379 (648)
CPU Time	10900	$\pm$40000	$>$ 50000	12500 (12900)	12700 (15900)

Table 18: Integrations statistics of EB, ROS2, BDF-2, IMEX RKC(fly) and IMEX RKC(full) running into steady state (performed on a Pentium IV 3.2 GHz). Surface chemistry is included. In IMEX RKC(fly) stability of the explicit part is controlled by the 'on the fly condition', whereas the full advection-diffusion stability condition is used in IMEX RKC(full). Number of F-evaluations for IMEX RKC are the ones containing reaction terms. The damping parameter in IMEX RKC is taken equal to $\varepsilon = 10$. If the results for damping parameter $\varepsilon = 1$ differ from the results for $\varepsilon = 10$, then they are given between brackets.

[4]For CPU times we keep on a region of 10% noise.

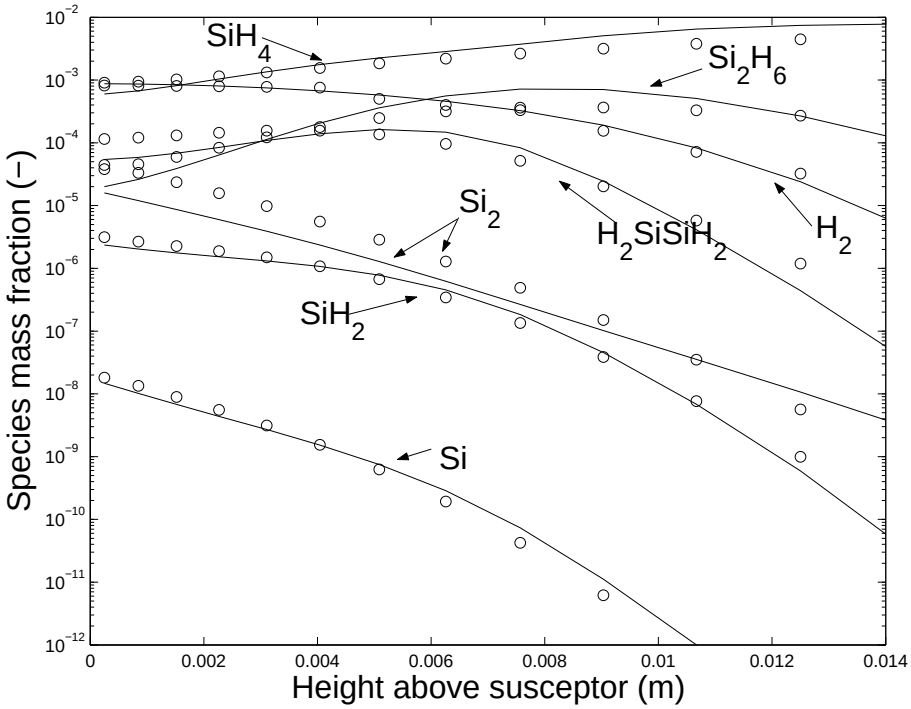

Figure 8: Steady state axial mass fraction profiles for some selected species; surface chemistry *not* included. A similar figure can be found in [8]. Solid lines: profiles obtained with the code of [8]. Circles: our steady state mass fraction profiles.

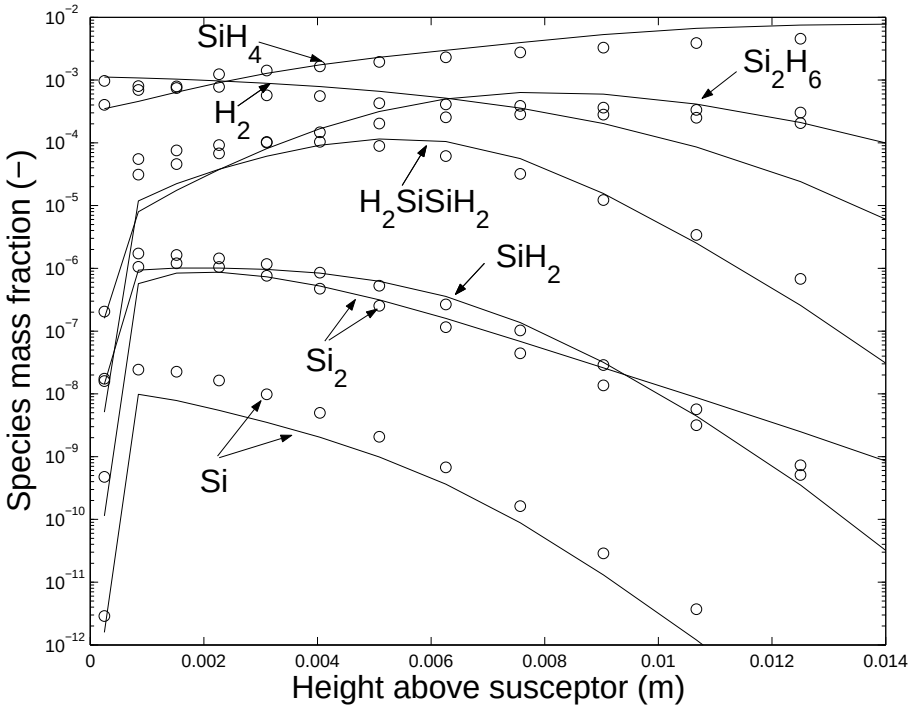

Figure 9: Steady state axial mass fraction profiles for some selected species; surface chemistry is included. A similar figure can be found in [8]. Solid lines: profiles obtained with the code of [8]. Circles: our steady state mass fraction profiles.

8 Conclusions

In this paper we presented two dimensional transient simulations of laminar reactive gas flows, that appear in Chemical Vapor Deposition. The accent has been put on time integration of the stiffly, nonlinearly coupled system of species equations, which describe the transport of mass within the reactor. Finding the (transient) solution of the equations describing the gas flow and transport of energy is a rather trivial task in comparison with solving the species equations. Therefore, we assume that these equations are already solved and the solutions are available.

We tested a collection of time integration methods, which are suitable for integration of stiff ODEs, and have good properties with respect to the conservation of positivity. Spatial discretization has been done in a positive way by a hybrid finite volume scheme. The nonlinear and linear solvers are not individually optimized for each ODE method. Actually, standard techniques are used to solve the nonlinear systems. Based on our experiments we conclude that the unconditionally positive Euler Backward scheme is the most efficient time integrator, in terms of total computational costs. However, for 3D transient simulations the, conditionally positive, IMEX RKC scheme is still an excellent candidate, because the associated non linear systems can be solved in a cheaper way. Other higher order, conditionally positive, time integration methods are computationally more expensive than Euler Backward and IMEX RKC.

Acknowledgments

Thanks are addressed to Dr. B.P. Sommeijer from the CWI in Amsterdam for his suggestions to improve the performance of our IMEX RKC code.

References

[1] E. Anderson, Z. Bai, C. Bischof, J. Demmel, J. Dongarra, J. Du Croz, A. Greenbaum, S. Hammarling, A. McKenney, S. Ostrouchov, and D. Sorensen, *LAPACK Users' Guide*, 2nd Ed., SIAM, Philadelphia, (1995)

[2] M.E. Coltrin, R.J. Kee, G.H. Evans, *A Mathematical Model of the Fluid Mechanics and Gas-Phase Chemistry in a Rotating Chemical Vapor Deposition Reactor*, J. Electrochem. Soc., 136, pp. 819-829, (1989)

[3] M.L. Hitchman and K.F. Jensen, *Chemical Vapor Deposition - Principles and Applications*, Acad. Press, London, (1993)

[4] W. Hundsdorfer and J.G. Verwer, *Numerical Solution of Time-Dependent Advection-Diffusion-Reaction Equations*, Springer Series in Computational Mathematics, 33, Springer, Berlin, (2003)

[5] C.R. Kleijn, *Transport Phenomena in Chemical Vapor Deposition Reactors*, PhD thesis, Delft University of Technology, Delft, (1991)

[6] C.R. Kleijn and Ch. Werner, *Modeling of Chemical Vapor Deposition of Tungsten Films*, Birkhäuser, Basel, (1993)

[7] C.R. Kleijn, *Chemical Vapor Deposition Processes*, in: M. Meyyappan, Computational Modeling on Semiconductor Processing, Artech House, Boston, pp. 97-229, (1995)

[8] C.R. Kleijn, *Computational Modeling of Transport Phenomena and Detailed Chemistry in Chemical Vapor Deposition- A Benchmark Solution*, Thin Solid Films, 365, pp. 294-306, (2000)

[9] B.P. Sommeijer, L.F. Shampine and J.G. Verwer, *RKC: An Explicit Solver for Parabolic PDEs*, J. Comput. Appl. Math. 88, pp. 315-326, (1997)

[10] TNO CVD-X user manual, Version 4.0, TNO Science and Industry, `support.glassgroup@tno.nl`

[11] S. van Veldhuizen, *Efficient Solution Methods for Stiff Systems of Advection-Diffusion-Reaction Equations, Literature Study*, Technical Report at the Delft University of Technology, Report 05-05, Delft, (2005)

[12] S. van Veldhuizen, C. Vuik and C.R. Kleijn, *Numerical Methods for CVD Simulation*, Technical Report at the Delft University of Technology, Report 06-07, Delft, (2006)

[13] J.G. Verwer and B.P. Sommeijer, *An Implicit-Explicit Runge-Kutta-Chebyshev Scheme for Diffusion-Reaction Equations*, SIAM Journal on Sci. Comp., 25, pp.1824-1835, (2004)

[14] J.G. Verwer, B.P. Sommeijer and W. Hundsdorfer, *RKC Time-Stepping for Advection-Diffusion-Reaction Problems*, Journal of Comp. Physics, 201, pp. 61-79, (2004)

[15] P. Wesseling, *Principles of Computational Fluid Dynamics*, Springer Series in Computational Mathematics, 29, Springer, Berlin, (2001)